

# Intra-hour cloud index forecasting with data assimilation

Travis M. Harty<sup>a,\*</sup>, William F. Holmgren<sup>b</sup>, Antonio T. Lorenzo<sup>b</sup>, Matthias Morzfeld<sup>a,c</sup>

<sup>a</sup>University of Arizona, Program in Applied Mathematics, 617 N. Santa Rita Ave., Tucson, AZ 85721, United States

<sup>b</sup>University of Arizona, Department of Hydrology & Atmospheric Sciences, 1133 E. James E. Rogers Way, Tucson, AZ 85721, United States

<sup>c</sup>University of Arizona, Department of Mathematics, 617 N. Santa Rita Ave., Tucson, AZ 85721, United States

---

## Abstract

We introduce a computational framework to forecast cloud index (CI) fields for up to one hour on a spatial domain that covers a city. Such intra-hour CI forecasts are important to produce solar power forecasts of utility scale solar power and distributed rooftop solar. Our method combines a 2D advection model with cloud motion vectors (CMVs) derived from a mesoscale numerical weather prediction (NWP) model and sparse optical flow acting on successive, geostationary satellite images. We use ensemble data assimilation to combine these sources of cloud motion information based on the uncertainty of each data source. Our technique produces forecasts that have similar or lower root mean square error than reference techniques that use only optical flow, NWP CMV fields, or persistence. We describe how the method operates on three representative case studies and present results from 39 cloudy days.

*Keywords:* Data assimilation, Ensemble forecast, Advection, Geostationary satellite, Optical flow, NWP

---

## 1. Introduction

Power grid management requires that solar power generation be predicted accurately (Kleissl, 2013). Intra-hour solar power forecasts require accurate predictions of clouds on small spatial and temporal scales. Forecasting on intra-hour time scales requires computationally efficient methods (an intra-hour forecast that takes more than a few minutes to compute is not useful).

We describe a computational framework for intra-hour cloud index (CI) forecasts based on a 2D advection model with random perturbations. We study a region, centered on Tucson, AZ, that contains 385 MW of solar power capacity (TEP, 2018). The advection of CI is driven by cloud motion vectors (CMVs) from satellite images and a mesoscale numerical weather prediction (NWP) model that are combined using data assimilation (DA). We use DA to assimilate CMVs derived from optical flow (Horn and Schunck, 1981; Lucas and Kanade, 1981), applied to successive geostationary satellite images every 15 minutes and CMV

fields derived hourly from a mesoscale NWP model. These two data sources are assimilated into a background ensemble that is initialized with a NWP CMV field. We refer to the system as ANOC for the **A**ssimilation of **N**WP winds and **O**ptical flow **C**MV<sub>s</sub>.

Generically, DA is a Bayesian technique to update numerical models using sparse and noisy observations (Reich and Cotter, 2015; Asch et al., 2016). We use an ensemble Kalman filter (EnKF) (see, e.g., Evensen (2009)) to perform our assimilations. EnKFs are computational tools for DA where forecast uncertainty is represented by an ensemble.

Optical flow is a method to determine a velocity field from consecutive scalar fields. Numerical methods for optical flow can be divided into two categories: dense optical flow (Horn and Schunck, 1981), where an entire vector field is produced, and sparse optical flow (Lucas and Kanade, 1981), where point estimates of a vector field are produced. We use both dense and sparse optical flow to determine CMVs in this study.

Advection of satellite-derived cloud properties for intra-hour CI or irradiance field forecasts for solar power applications has been considered in several

---

\*Corresponding author

Email address: travisharty@math.arizona.edu  
(Travis M. Harty)

studies (Kleissl, 2013). A mean squared error minimization method (Lorenz et al., 2004; Wolff et al., 2016), optical flow (Nonnenmacher and Coimbra, 2014; Peng et al., 2013), neural networks (Côté and Tatnall, 1995) and a Monte Carlo method (Hammer et al., 1999) have been used to derive CMVs from successive cloud images. Advection based forecasts with CMV fields derived from NWP models are described in Miller et al. (2012, 2017); Descombes et al. (2014). The ANOC system we describe in this paper uses DA to combine CMVs from an NWP model and CMVs derived from optical flow.

Previous works also explore combinations of different irradiance forecasts. For example, (Wolff et al., 2016) use support vector regression to generate irradiance forecasts from a combination of ground measurements, satellite advection via CMV fields, and NWP irradiance forecasts. Haupt et al. (2018), combine several different irradiance forecasting models (statistical methods based on surface measurements, satellite advection, NWP) using the statistics of the historical performance of each of the different forecasting methods.

Meteorologists use DA to assimilate CMVs into NWP models as observations of atmospheric flow. These CMVs are often obtained using a cross-correlation or mean squared error minimization method and are most useful over remote regions, e.g. oceans, where direct observations are not available (Menzel, 2001; Nieman et al., 1997).

The ANOC system uses DA with a conceptually intuitive and computationally inexpensive 2D advection model. The 2D advection model produces forecasts that are easy to understand and allows for DA to be implemented in a clear way. The computational savings compared to a full 3D model allows us to forecast at shorter time scales and also allows for ensemble forecasts and ensemble based DA. This allows us to assimilate CMV data into our ensemble taking the certainty in each source of data into account. This approach is inspired by Lorenzo et al. (2017) where DA is used to combine ground sensors with clear-sky index fields derived from geostationary satellite images.

The remainder of the paper is organized as follows. In Section 2 we introduce the satellite imagery and NWP model we use. In Section 3 we describe the operation of the ANOC system. In Section 4 we briefly describe reference forecast that we compare to the ANOC system. In Section 5 we describe how ANOC functions in the context of three case studies. In Section 6 we present results

computed over 39 days. Section 7 contains our concluding remarks.

## 2. Satellite imagery and numerical weather model

The ANOC forecasting system combines geostationary satellite images and winds from a mesoscale NWP model. The domain of interest is 40 km from west to east and 56 km from south to north containing Tucson, AZ (see Section 3). To produce forecasts in this domain of interest, we consider an area centered on Tucson, AZ, that is 360 km on each side. We study the time period of April, May, and June 2014, with each day starting at 16:30 UTC (9:30 MST) and ending at 22:30 UTC (15:30 MST).

### 2.1. Satellite data

We use images taken by the GOES-15 geostationary satellite located in the GOES-West position. Satellite images are usually available every 15 minutes, though the time between satellite images is sometimes longer. For simplicity, we will refer to satellite images being available every 15 minutes. We use the visible band at a spatial resolution of approximately 1 km. The latitude and longitude coordinates of the satellite image are converted to kilometers with the Lambert conformal conic projection (Snyder, 1987). The result is interpolated onto a regular square 1 km<sup>2</sup> grid with nearest neighbor interpolation. The satellite images are downloaded from the Comprehensive Large Array-data Stewardship System (CLASS) (NOAA, 2018). Animations of the satellite images are available in Harty (2018).

The pixel values of a satellite image are converted into CI following in part the methods described in Perez et al. (2002). First, the pixel value is normalized:

$$\text{norpix} = \text{pix} \cdot \text{am} \cdot \text{soldist}, \quad (1)$$

where *pix* is the raw satellite pixel, *am* is the absolute airmass, and *soldist* is the Earth-Sun distance in astronomical units. The normalized pixel value (*norpix*) is converted into a cloud index (CI) value:

$$\text{CI} = \frac{\text{norpix} - \text{low}}{\text{high} - \text{low}}, \quad (2)$$

where *high* is equal to the mean of the 20 highest *norpix* values over a three months window, and *low* is calculated as follows. The method presented in

Perez et al. (2002) uses one value for *low* for the entire day. We modify the method and use different values for *low* throughout the day to remove additional surface albedo. For each time of day, *low* for that time is calculated as the mean of the 40 lowest norpix values for that time of day over the same three month window as high. When calculating *low* and *high* we use all three months of satellite data, meaning that the resulting CI fields could not have been used to create true forecasts. This problem can be mitigated by using a sliding window of past satellite images to calculate *high* and *low* (as is done in Perez et al. (2002)), rather than using the full three months of satellite images. We do not do so here because we anticipate only minor differences, and because it would require more data and computation.

After calculating the CI field, it is linearly interpolated onto a square grid with a resolution of  $250\text{ m}^2$  that is used in ANOC for 2D advection.

### 2.2. Numerical weather prediction model

We use the wind and relative humidity fields from the operational forecasts of the University of Arizona Department of Hydrology and Atmospheric Sciences. The forecast system uses the Weather Research and Forecasting (WRF) model with an outer domain covering the western US with a 5.4 km horizontal grid spacing, and an inner domain covering Arizona with a 1.8 km horizontal grid spacing. We use forecasts that are initialized at 12Z with the Global Forecast System (GFS) data produced by the National Centers for Environmental Prediction (NCEP). We use this model because it is readily available to us, but we expect our approach will perform similarly with a different mesoscale NWP model.

## 3. The ANOC forecast system

We summarize the operation of the **A**ssimilation of **N**WP winds and **O**ptical flow **C**MVs system (ANOC). The ANOC system uses an ensemble of size 20. Each ensemble member consists of a CI field and a corresponding CMV field with  $u$  (west to east) and  $v$  (south to north) components over a given spatial domain (see Section 3.1). A 2D advection model advects the CI component of each ensemble member using the CMV component of the ensemble member (see Section 3.2). The CMV information is derived from sparse optical flow (see

Section 3.3), as well as from the NWP model (see Section 3.4). DA is used to combine these two sources of information with the CMV component of the ensemble (see Section 3.5).

The ANOC system is started every day at 16:30 UTC (9:30 MST) with an initial ensemble (see Section 3.6). The system runs until 22:30 UTC (15:30 MST). Using satellite images from this window (centered around solar noon) eliminates time periods with low solar elevation angles that could complicate this proof of principle study. A detailed overview of the ANOC forecast system is shown in Fig. 1.

### 3.1. ANOC domain and computational domain

ANOC produces CI forecasts for a region centered around Tucson, AZ, whose sides are 40 km from west to east and 56 km from south to north. The computational domain includes the region around Tucson and is defined to be large enough to avoid the advection of boundary artifacts into the domain at the maximum wind speed and longest forecast horizon. The size of the computational domain thus depends on the wind velocities. To define the computational domain for a given day we find the maximum wind speed in the four cardinal directions, as forecasted by the NWP model, in a domain that is centered on Tucson, AZ, and 360 km on both sides. These maximum wind speeds, along with the longest forecast horizon, allows us to determine how much larger the computational domain must be in each direction than the ANOC domain. Figure 2 illustrates the computational domain and the domain of interest for May 29, 2014. On this day, the winds are stronger in the north-south than in the east-west direction. As a result, the computational domain is larger in the north-south than in the east-west direction.

### 3.2. Advection model and random perturbations

In ANOC, predictions of CI are based on a 2D advection model with open boundaries. Random perturbations are added to the CI and CMV fields to account for data and model errors. In particular our framework does not allow for cloud growth or convection.

The advection equation is

$$\frac{\partial \psi}{\partial t} = -\nabla \cdot (\mathbf{C}\psi), \quad (3)$$

$$\psi(0) = \psi_0$$

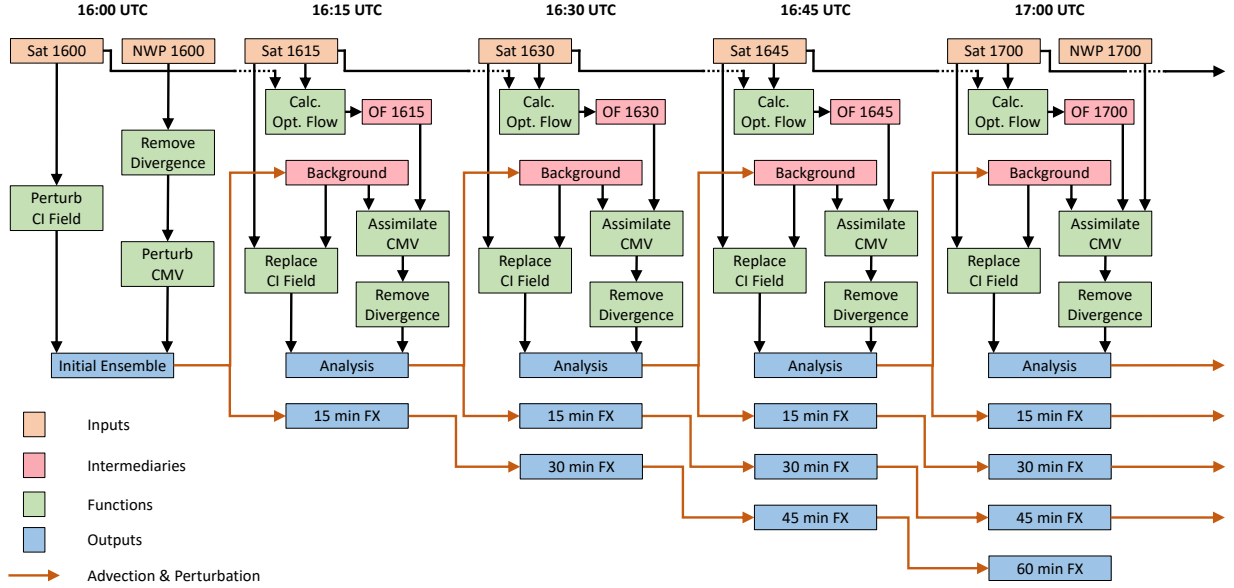


Figure 1: This figure shows a schematic of the initialization and initial operation of the ANOC system. We illustrate input data (satellite images and NWP wind fields) in orange, intermediaries (optical flow CMVs and background ensemble) in pink, functions (assimilating CMV fields, removing divergence, etc.) in green, and outputs (analysis ensemble and forecasts) in blue. The system is initialized at 16:00 UTC with an initial satellite image (Sat 1600) and NWP CMV field (NWP 1600). The divergence is removed from the NWP CMV field, then the fields are randomly perturbed to form the initial ensemble. This initial ensemble and its mean are advected for 15 minutes (represented by orange arrows) producing a 15 minute forecast ensemble and the corresponding control forecast (15 min FX). This process is repeated three more times creating 30, 45, and 60 minute forecast ensembles for time periods 16:30, 16:45, and 17:00. In addition to the control forecast that is created by advecting the ensemble mean (the analysis after assimilation), the mean of the advected ensemble is also used as a forecast. The 15 minute forecast ensemble is also a background ensemble (Background) into which new data are assimilated. At the 16:15 time period, a new satellite image (Sat 1615) is available. Two consecutive satellite images (Sat 1600 and Sat 1615) are used to calculate sparse optical flow vectors (OF 1615), that are assimilated into the background CMV field. While the optical flow CMVs and background ensemble are outputs of calculations, they are inputs to the DA system. Divergence is removed from the resulting CMV field and the CI field from the current satellite image (Sat 1615) replaces the background CI fields. This results in the analysis ensemble (Analysis). The above process is then repeated with the analysis ensemble rather than the initial ensemble. The entire cycle repeats until a predetermined stopping time. There is a slight change at time period 17:00 when a new NWP CMV field is available (NWP 1700). The only difference for this time, and all other times when NWP CMV fields are available, is that the NWP CMV field is assimilated into the CMV component of the background ensemble in addition to the sparse optical flow CMVs.

where  $\psi(t)$  is the 2D CI field at time  $t$ ,  $\psi_0$  is the initial CI field, and  $\mathbf{C} = (u, v)$  is the CMV field. We solve Eq. (3) using a third-order Runge-Kutta method in time and a fourth order spatial derivative described in Wicker and Skamarock (2002). To increase the effective resolution of the advected grid we perform the advection on a 250 m grid. Furthermore, to prevent dispersion of sharp cloud edges in the field, we linearly interpolate the CI field to the 250 m grid. This has the effect of a smoother transition from cloud to clear sky, while maintaining a sharp cloud edge at the original resolution of the satellite image. The time step of each advection is calculated every 15 model minutes using

$dt = (0.7)(250)(u_{max} + v_{max})^{-1}$ , where  $u_{max}$  and  $v_{max}$  are the maximum wind speeds in each direction in meters per second.

We keep the CMV fields, that are updated by a DA cycle every hour, divergence free (see Fig. 1). Whenever an operation introduces divergence (assimilating sparse optical flow or NWP CMV fields) we remove it as follows. The CMV field,  $\mathbf{C}$ , is decomposed into a divergence-free component,  $\tilde{\mathbf{C}}$ , and a component that has non-zero divergence. The non-zero divergence component is the gradient of a scalar field  $\phi$ :

$$\tilde{\mathbf{C}} = \mathbf{C} + \nabla\phi. \quad (4)$$

We obtain  $\nabla\phi$ , and therefore  $\tilde{\mathbf{C}}$ , by solving Pois-

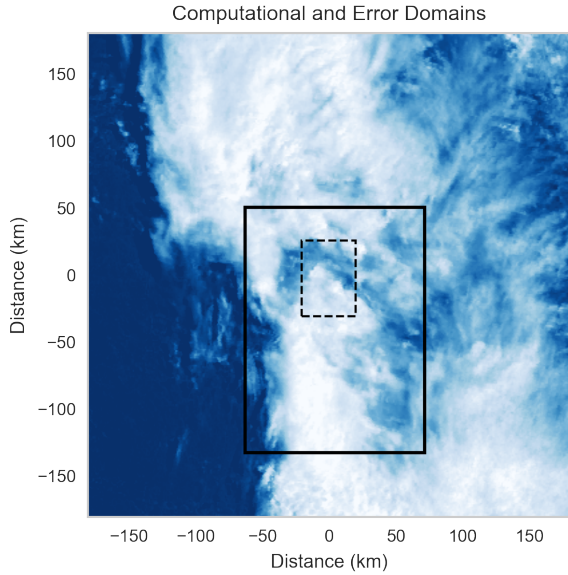


Figure 2: CI field derived from a geostationary satellite image on May 29, 2014. The area shown is a square with 360 km sides, centered on Tucson, AZ. The solid line describes the computational domain (for this day) over which CI fields are advected and DA is performed. The smaller domain, surrounded by a dashed line, is the area over which forecasts are produced and is approximately the Tucson, AZ, region. The whole image is the domain over which the average relative humidity is calculated in order to select a vertical level from the NWP model.

son’s equation. We use Neumann boundary conditions for numerical efficiency and solve the Poisson problem using a finite element solver implemented in the FEniCS package (Alnæs et al., 2015; Logg et al., 2012).

After every 5 minutes of modeled advection, each ensemble member’s CI and CMV fields are randomly perturbed. To perturb the CI fields, we first identify the cloudy areas of the CI field. This is done by defining a “target field” which is equal to one in cloudy areas and decays to zero (logistic decay) in clear areas. The target field is multiplied element wise (Schur or Hadamard matrix product) by a Gaussian random field (GRF). Each element of the GRF has a mean of zero and standard deviation of 0.03 CI. The GRF has a squared exponential correlation function with a length scale of 5 km. The standard deviation and correlation function are tunable parameters that are chosen to produce reasonable CI fields. The product of target and random fields is added to the ensemble member’s CI field. This has the effect of perturbing the

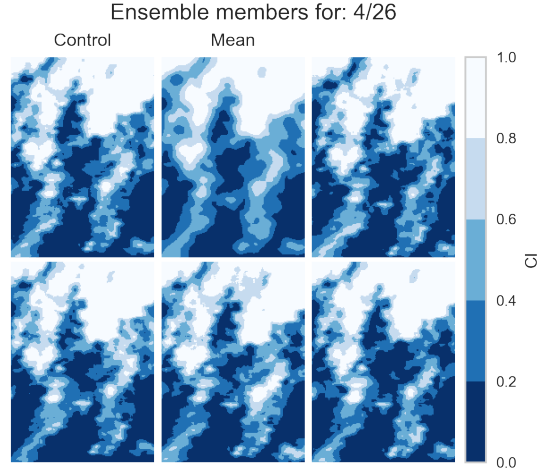


Figure 3: 30 minute CI forecast for April 26, 2014, at 13:00 MST. This figure shows the CI fields of four ensemble members, the ensemble mean of all 20 members, and the control forecast (see Section 3.5). Ensemble members are different due to random perturbations of the CI and CMV fields. The ensemble mean is smoother than an individual ensemble member, but the control forecast is not.

cloudy areas of the CI field while leaving the clear areas unchanged.

To perturb the CMV component of the ensemble, we generate a stream function using a GRF. Each element of the GRF has a mean of zero and standard deviation of  $1 \text{ m}^2 \text{ sec}^{-1}$ . The GRF has a squared exponential correlation function with a length scale equal to 50 km. After calculating the corresponding 2D vector field,

$$U = \frac{\partial \phi}{\partial y}, V = -\frac{\partial \phi}{\partial x}, \quad (5)$$

where  $\phi$  is the random stream function, the resulting  $U$  and  $V$  random CMV fields are then multiplied by 0.25 resulting in a standard deviation of  $0.25 \text{ m sec}^{-1}$  for each element of each field. The stream functions generate random, divergence-free CMV fields which are added to the CMV component of the ensemble. The parameters that define the CMV perturbations are tunable and chosen to produce reasonable CMV fields and resulting CI fields.

The CI fields of four ensemble members, the ensemble mean of all 20 members, and the control forecast (see Section 3.5) are shown in Fig. 3. The differences between the ensemble members are a result of the random perturbations and assimilating CMVs from optical flow (see Section 3.3).

### 3.3. CMV observations from sparse optical flow

Optical flow is a method to determine a velocity field from consecutive scalar fields. The optical flow method relies on the assumption that the positions of individual elements of the field move, but the field values remain unchanged. The sparse optical flow method of Lucas-Kanade (Lucas and Kanade, 1981) identifies a set of points in the first of two images where the gradient is large in orthogonal directions. This set of points is tracked to the next image and, once the points are located in the next image, the vectors that connect the set of points in the first and second images define the velocity field at these points in the second image.

We use this technique, implemented as described in Bradski (2000), to compute CMVs based on two consecutive satellite images. The CMVs derived from sparse optical flow are assimilated as “CMV observations” (see Section 3.4 and Fig. 1). The number of CMV observations, as well as their location, changes from image to image (every 15 minutes).

### 3.4. CMV observations from an NWP model

The ANOC forecasting system uses 2D advection and we assume that there is only one cloud level with clouds moving with the wind. These assumptions are often violated (see, e.g., the case study with two distinct cloud layers in Section 5.3) but allow for an easily understandable and computationally inexpensive forecasting process.

The NWP model we use has 38 vertical levels. Following Lave and Kleissl (2013), we use the winds from the vertical level with the highest mean relative humidity over an area that is 360 km on each side and centered on Tucson, AZ. We use the  $u$  (west to east) and  $v$  (south to north) components of the wind field in the selected vertical layer (neglecting motion in the vertical direction). The two wind components are interpolated using nearest neighbor to a 1 km Arakawa-C grid. We then linearly interpolate to the 250 m grid used for advection. The resulting 2D wind field is smoothed by a Gaussian filter with a standard deviation of 15 km. This level of smoothing is found through trial and error to reduce forecast error.

### 3.5. Data assimilation and forecasting

We use an ensemble Kalman filter (EnKF) to assimilate CMV observations from sparse optical flow (every 15 minutes) and CMV fields from the NWP

model (every hour) into the CMV component of the ensemble (see Fig. 1). An EnKF uses a numerical model to generate a “background” ensemble and, using the observations, updates the background to an analysis ensemble (see, e.g., Evensen (2009)). The analysis ensemble is used to generate forecasts at horizons of 15, 30, 45, and 60 minutes. Thus, the ANOC system produces a forecast *ensemble* rather than a *single* CI forecast. A single forecast can be obtained, for example, by computing the ensemble mean.

Another single forecast can be generated by advecting (without random perturbations) the analysis mean. This forecast is called the control forecast. The ensemble mean forecast tends to be smoother than the control forecast or individual ensemble members, but also tends to have higher skill (Kalnay, 2003) even after accounting for the additional smoothing (Toth and Kalnay, 1997). The control forecast, however, maintains sharper cloud edges that are important for forecasting how quickly solar power output will change. Our approach parallels that of contemporary operational NWP ensemble systems.

Two implementations of EnKF are used in ANOC. We use the stochastic ensemble Kalman filter (Burgers et al., 1998) to assimilate sparse optical flow CMVs and the Local Ensemble Transform Kalman Filter (LETKF) (Hunt et al., 2007) to assimilate CMV fields from the NWP model. We make these choices because of computational considerations. Assimilating the CMV fields from the NWP model is a high-dimensional problem because we assimilate a large number of observations on a large domain. The LETKF is an efficient DA technique for high-dimensional problems. Assimilating the CMVs from optical flow is a low-dimensional problem because the number of observations is small. The stochastic EnKF can handle this task and is easy to implement and to tune.

The EnKFs require that we define an observation error covariance matrix,  $\mathbf{R}$ . For optical flow CMVs and NWP CMV fields,  $\mathbf{R}$  is diagonal, i.e., errors are assumed to be independent. This is common when the only source of error in an observation comes from instrument noise (Kalnay, 2003). Though this is not the case for the data we assimilate, it is a convenient assumption for this preliminary study. The diagonal elements of  $\mathbf{R}$  are the squares of error standard deviations. The error standard deviations are constant and equal to  $1 \text{ m sec}^{-1}$  for optical flow CMVs and equal to  $8 \text{ m sec}^{-1}$  for NWP CMV fields.

These values for  $\mathbf{R}$  are chosen through trial and error to produce forecasts with low root mean square error (RMSE, see Section 4.6 for a precise definition).

The ensemble size for the EnKFs is 20 (one could, however, also consider larger ensemble sizes). This means that computed sample covariance matrices, used during DA, contain large sampling error. Localization and inflation are two tools to account for this sampling error (Evensen, 2009). Localization reduces spurious correlations due to a small ensemble size and inflation enlarges the covariance matrix because covariances computed with a small ensemble size are typically underestimated.

The parameters that define the localization and inflation are tuned. We consider 36 different sets of these parameters and, for each one, run ANOC for three days that are carefully chosen to represent different weather conditions. We choose April 15, 2014, which is characterized by zonal flow (see Section 5.1), May 29, 2014, which is characterized by a short wave trough (see Section 5.2), and June 11, 2014, which is characterized by shallow convection and zonal flow. We determine which localization/inflation parameters lead to the smallest RMSE for each day and only find minor differences between the three days (see Section 4.6 for a precise definition of RMSE). We then declare the set of parameters that leads to the smallest RMSE on average over the three days to be optimal and use these parameters throughout this paper.

### 3.6. Initial ANOC ensemble

The CMV component of the initial ensemble is generated as follows. We obtain a CMV field from the NWP model (see Section 3.4) and perturb it by adding a random number from a normal distribution with mean zero and standard deviation  $1 \text{ ms}^{-1}$ . The CI component of the initial ensemble is derived from the satellite image at 16:30 UTC that is perturbed by random scaling. This is done by linearly rescaling the CI values from a range of  $[0, 1]$  to  $[\text{min}, \text{max}]$  where min is drawn from a normal distribution with mean zero and standard deviation 0.04 and max is drawn from a normal distribution with mean one and standard deviation 0.2.

### 3.7. Computational requirements of ANOC

Each day's forecast has a different run time because different wind conditions lead to differently sized computational domains. On May 29, 2014

(also discussed in Section 5.2), a one hour long forecast requires approximately 5.5 minutes. Approximately 2% of the time is spent assimilating NWP CMV fields, 2% of the time is spent assimilating sparse optical flow CMVs, 34% of the time is spent advecting and perturbing, and 64% of the time is spent removing divergence from the ensemble's CMV fields. The large proportion of time spent on removing divergence (solving a Poisson problem) can be reduced, but we do not pursue this problem here. The above run time for the ANOC system was found on a virtual machine allocated 32 of 48 virtual cores coming from two Intel Xeon E5-2690 v3 processors each with 12 cores (24 virtual cores with hyper threading) with a base frequency of 2.6 GHz.

## 4. Reference forecasts

In this section we describe reference forecast systems that will be used to validate the ANOC forecast in later sections. None of the reference forecast systems use ensembles or DA. These systems, however, are intuitive and some are in use. Later on (Sections 5 and 6), these methods will serve as benchmarks to assess the utility of ANOC with a set of performance metrics, described at the end of this section.

All reference forecast systems (except persistence) estimate CMV based on one source of information (satellite imagery, a NWP model or a radiosonde) and use ANOC's 2D advection model (without random perturbations) for the CI forecast. For each forecast system, we explain how many CMVs are used and how often these are updated during a six hour forecasting day. This should be compared to the ANOC system that uses  $N \times M \times 6 \times 4 \times 20$  vectors for one day's forecasts assuming a computational domain of size  $N \times M$ , six hours of forecasts, a new satellite image every 15 minutes, and 20 ensemble members.

### 4.1. Persistence forecast

In the persistence forecast the CI derived from one satellite image (see Section 2.1) is used as the 15, 30, 45, and 60 minute forecast. The forecasts are updated every 15 minutes when a new satellite image becomes available. The persistence forecast is intuitive and accurate on short time horizons, but less accurate for longer horizons. No vectors are used to produce this forecast because it does not make use of a CMV field.

510 *4.2. Radiosonde forecast*

The radiosonde forecast uses the TWC 12Z radiosonde measurements of winds in  $u$  and  $v$  directions at the level with the highest relative humidity, see also Lave and Kleissl (2013); Guillot et al. (2012). The  $u$  and  $v$  winds are used over the entire domain and for the entire day. Every 15 minutes, the CI field derived from a satellite images is advected using these winds and the 2D advection (without random perturbation) of ANOC. For one six hour day, this forecast uses one vector to describe the CMV field.

520 *4.3. Forecast based on the spatial average of NWP winds*

The forecast based on the spatial average of NWP winds uses the spatial average of the  $u$  and  $v$  wind components of the NWP model at the vertical layer described in Section 3.4. The NWP winds are updated hourly, therefore this forecast updates the CMV field every hour. For one six hour day, this forecast uses six vectors to describe the CMV field.

530 *4.4. Forecast based on NWP winds*

Winds from the NWP model, as described in Section 3.4, are used to generate a divergence-free CMV field. This technique uses the NWP model winds that are updated hourly, therefore the CMV field is updated every hour. For one six hour day and an  $N \times M$  advection domain, this forecast uses  $N \times M \times 6$  vectors to describe the CMV field.

540 *4.5. Dense optical flow forecast*

We use dense optical flow applied to consecutive satellite images to generate a CMV field (see also Nonnenmacher and Coimbra (2014)). We use the dense optical flow method of Horn-Schunck (Horn and Schunck, 1981), implemented as described in Sun et al. (2010). The Horn-Schunck method is a variational technique that includes a smoothness constraint on the dense vector field. One effect of this smoothness constraint is that portions of the image that do not contain points to be tracked (because the image gradient is uniform) assume values from neighboring regions.

The CMV field is updated when a new satellite image becomes available (every 15 minutes). We remove divergence from the CMV field before producing a CI forecast with the 2D advection model (without random perturbations) of ANOC. For one six hour day and an  $N \times M$  advection domain, this

forecast uses  $N \times M \times 6 \times 4$  vectors, assuming a new satellite image every 15 minutes, to describe the CMV field. Dense optical flow creates CMV vectors at every point in the image. This is in contrast to sparse optical flow, used in ANOC, that generates CMVs only at points that are easily tracked.

565 *4.6. Performance metrics*

Comparisons of the various forecast systems use the following performance metrics for the CI field forecasts:

- (i) Root Mean Square Error (RMSE) of a CI forecast and the CI field derived from a satellite image.
- (ii) The Pearson correlation coefficient (Corr.) between the CI forecast and the CI field derived from a satellite image.
- (iii) Bias between the CI forecast and the CI field derived from a satellite image.
- (iv) RMSE Skill Score, with the persistence forecast serving as the reference forecast ( $SS_{\text{per}}$ ).

To compute the performance metrics, we use the time series of CI generated by a forecast system ( $X_f$ ) and the time series of CI derived from the satellite images ( $X_T$ ), both over the domain of interest, as described in Section 3.1. These time series are of shape  $(N_x, N_y, N_t)$  where  $N_x$  and  $N_y$  are the side lengths of the domain of interest, and  $N_t$  is the number of time periods being compared. For computations, we reshape the arrays into one dimensional vectors  $x_f$  and  $x_T$ , each of size  $N = N_x N_y N_t$ . With this notation, the performance metrics are defined as:

$$\text{RMSE} = \sqrt{\frac{1}{N} \sum_{i=1}^N (x_{i,f} - x_{i,T})^2}, \quad (6)$$

$$\text{Corr.} = \frac{\sum_{i=1}^N (x_{i,f} - \bar{x}_f)(x_{i,T} - \bar{x}_T)}{\sqrt{\sum_{i=1}^N (x_{i,f} - \bar{x}_f)^2} \sqrt{\sum_{i=1}^N (x_{i,T} - \bar{x}_T)^2}}, \quad (7)$$

$$\text{Bias} = \frac{1}{N} \sum_{i=1}^N (x_{i,f} - x_{i,T}), \quad (8)$$

and,

$$SS_{\text{per}} = 1 - \frac{\text{RMSE}_f}{\text{RMSE}_{\text{per}}}, \quad (9)$$

where  $x_{i,f}$  and  $x_{i,T}$  are the  $i^{\text{th}}$  entry of  $x_f$  and  $x_T$ ,  $\bar{x}$  is the average of  $x$ ,  $\text{RMSE}_f$  is the RMSE of a



595 forecast, and  $\text{RMSE}_{\text{per}}$  is the RMSE of the persistence reference forecast. Further discussion of these metrics can be found in Wilks (2011).

## 5. Case studies

600 We describe how ANOC operates and how it compares to reference forecasting systems in the context of three case studies that represent typical weather conditions for Tucson, AZ.

### 5.1. Case Study 1: Zonal flow

605 The first day we explore, April 15, 2014, is dominated by zonal flow without convection. The clouds are cirrus with low CI values, mostly less than 0.6 CI, and do not exhibit much dissipation or growth. The 12Z radiosonde reports a relative humidity peak near 11 km where the wind speed is  $30 \text{ ms}^{-1}$ . For this day, the essential assumptions of the ANOC, dense optical flow, and NWP winds forecast systems are satisfied and we expect these methods to produce similar forecasts.

615 The performance metrics are shown in Table 1. Bold type highlights the smallest errors and highest correlation. As expected all forecast systems, apart from persistence and radiosonde forecast systems, perform similarly on this day. The ANOC forecasts, however, have lower RMSEs and higher correlations than the other forecast systems for all horizons. Moreover, at 45 and 60 minute horizons the ANOC forecasts have significantly higher correlation than all other forecast systems.

625 Figure 4 shows RMSE as a function of forecast horizon of the ANOC ensemble, the ANOC ensemble mean and control, the dense optical flow forecast, the forecast using NWP winds, and the persistence forecast. For clarity, in Figs. 4, 5 and 7, the radiosonde forecast and the forecast based on the spatial average of NWP winds are not included. The RMSE of the individual ANOC ensemble members are all similar to the RMSE of the forecast based on NWP winds and the forecast based on dense optical flow for this day. The effect of averaging the ensemble members results in the ANOC ensemble mean forecast that has a lower RMSE than any of the other ensemble members. The ANOC control forecast has an RMSE lower than the individual ANOC ensemble members, but higher than the ensemble mean.

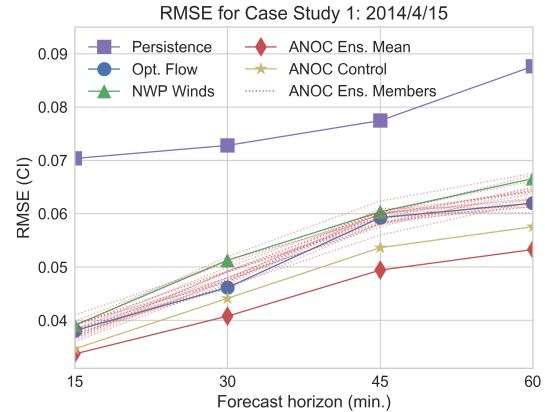


Figure 4: RMSE as a function of forecast horizon in Case Study 1 (zonal flow). Shown are RMSE of the ANOC ensemble, ANOC ensemble mean, ANOC control, and of two reference forecast systems. All forecast systems perform similarly on this day.

### 5.2. Case Study 2: Shortwave trough

645 The weather on May 29, 2014 is driven by a shortwave trough, moving from west to east. Local winds are strongest from south to north, with the wind field weaker but more variable in the west to east direction. The clouds on this day are a mixed variety of mid-altitude clouds. The clouds are significantly thicker than the clouds in Case Study 1, with many of the larger clouds having a CI value of around 1.0. There is also a larger amount of convection and a greater amount of cloud growth and dissipation. The 12Z radiosonde for this day shows a peak in relative humidity near 5.5 km where the wind speed is  $15 \text{ ms}^{-1}$ .

655 The performance metrics for the forecast systems are shown in Table 2. The ANOC ensemble mean and control have higher correlations and lower RMSEs than all other forecast systems. As in Case Study 1, the reduction in RMSE and the increase in correlation of the ANOC forecasts compared to the other forecast systems increases with the forecast horizon. This is illustrated in Fig. 5, where we show RMSE as a function of forecast horizon for the ANOC ensemble, ANOC ensemble mean, ANOC control, the forecast based on dense optical flow, the forecast based on NWP winds, and the persistence forecast. All ANOC ensemble members have comparable RMSE, that are also comparable to the forecast based on NWP winds, but lower than the forecast based on dense optical flow.

660 Figure 6, shows a typical forecast using the

Table 1: Performance metrics for Case Study 1, April 15, 2014, a day with cloud motion dominated by zonal flow. The units of RMSE and bias are CI. The highest correlation and lowest RMSE and bias for each forecast horizon are in bold type. The ANOC ensemble mean and control forecast have lower RMSEs and higher correlations than the reference forecasts, but all forecasts have low RMSE.

	Horizon	ANOC Ens. Mean	ANOC Control	Persis.	Opt. Flow	NWP Winds	NWP Avg. Winds	Radiosonde
RMSE	15	<b>0.03</b>	<b>0.03</b>	0.07	0.04	0.04	0.04	0.07
	30	<b>0.04</b>	<b>0.04</b>	0.07	0.05	0.05	0.05	0.08
	45	<b>0.05</b>	<b>0.05</b>	0.08	0.06	0.06	0.06	0.09
	60	<b>0.05</b>	0.06	0.09	0.06	0.07	0.06	0.09
Corr.	15	<b>0.85</b>	0.84	0.31	0.80	0.79	0.82	0.29
	30	<b>0.77</b>	0.73	0.29	0.70	0.62	0.67	0.20
	45	<b>0.68</b>	0.63	0.22	0.53	0.49	0.55	0.06
	60	<b>0.64</b>	0.57	0.06	0.48	0.37	0.46	0.08
Bias	15	<b>0.00</b>	<b>0.00</b>	-0.01	<b>0.00</b>	<b>0.00</b>	<b>0.00</b>	<b>0.00</b>
	30	<b>0.00</b>	<b>0.00</b>	-0.01	<b>0.00</b>	-0.01	<b>0.00</b>	<b>0.00</b>
	45	<b>-0.01</b>	<b>-0.01</b>	<b>-0.01</b>	<b>-0.01</b>	<b>-0.01</b>	<b>-0.01</b>	<b>-0.01</b>
	60	<b>-0.01</b>	<b>-0.01</b>	<b>-0.01</b>	<b>-0.01</b>	-0.02	<b>-0.01</b>	<b>-0.01</b>

Table 2: Performance metrics for Case Study 2, May 29, 2014, a day with weather conditions driven by a shortwave trough. The units of RMSE and bias are CI. The highest correlation and lowest RMSE and bias for each forecast horizon are in bold type. The ANOC ensemble mean and control forecasts have the lowest RMSE for all forecasts horizons. The forecast based on NWP winds has a lower RMSE than that based on dense optical flow for the 30, 45, and 60 minute horizons.

	Horizon	ANOC Ens. Mean	ANOC Control	Persis.	Opt. Flow	NWP Winds	NWP Avg. Winds	Radiosonde
RMSE	15	<b>0.15</b>	<b>0.15</b>	0.17	<b>0.15</b>	0.16	<b>0.15</b>	0.19
	30	<b>0.18</b>	<b>0.18</b>	0.22	0.20	0.19	0.19	0.26
	45	<b>0.17</b>	0.18	0.24	0.24	0.20	0.21	0.28
	60	<b>0.18</b>	0.19	0.27	0.28	0.21	0.21	0.30
Corr.	15	<b>0.88</b>	<b>0.88</b>	0.83	0.87	0.87	0.87	0.80
	30	<b>0.83</b>	0.82	0.73	0.81	0.81	<b>0.83</b>	0.62
	45	<b>0.84</b>	0.82	0.65	0.75	0.80	0.78	0.46
	60	<b>0.82</b>	0.81	0.54	0.71	0.79	0.78	0.37
Bias	15	<b>0.00</b>	<b>0.00</b>	0.03	-0.04	0.01	<b>0.00</b>	0.04
	30	<b>0.00</b>	<b>0.00</b>	0.06	-0.08	0.02	<b>0.00</b>	0.08
	45	-0.01	<b>0.00</b>	0.07	-0.14	0.02	-0.01	0.08
	60	-0.02	-0.01	0.08	-0.17	0.03	<b>0.00</b>	0.07

ANOC ensemble mean, dense optical flow and NWP winds along with corresponding errors. The forecast based on dense optical flow leads to large errors because it advects the cloud edge too far to the east and thins the clouds too much. These issues are reduced in the ANOC forecasts because the optical flow derived information is combined with the winds of the NWP model.

### 5.3. Case Study 3: Mid-latitude trough

The weather on April 26, 2014, is driven by a strong mid-latitude trough. Winds are blowing from the southwest to the northeast. There are two distinct cloud layers and clouds are a mixed variety of mid-altitude clouds as well as high-altitude cirrus. The cirrus clouds are moving at a significantly higher speed than the mid-altitude clouds: the 12Z radiosonde shows relative humidity peaks near 4 km and 10 km with respective wind speeds of  $20 \text{ ms}^{-1}$  and  $40 \text{ ms}^{-1}$ . Thus, this case study fea-

tures a two level cloud system and violates ANOC's assumption of a single cloud layer.

The performance metrics are listed in Table 3. As before, bold type highlights the smallest errors and highest correlation. The ANOC ensemble mean has lower RMSE and higher correlation than the other methods. Figure 7 shows RMSE as a function of forecast horizon of the ANOC ensemble, ensemble mean, and control as well as of the forecasts based on dense optical flow, NWP winds, and the persistence forecast. In contrast to Case Study 2, we find that RMSE of the forecast based on NWP winds is higher than RMSE of the forecast based on dense optical flow. The relative reduction in RMSE of the forecast based on dense optical flow compared to the forecast based on NWP winds, however, decreases with the forecast horizon, i.e., on time scales that are more appropriate for the NWP model.

Forecasts of the ANOC ensemble mean, dense optical flow, and NWP winds are shown in Fig. 8. The

Table 3: Performance metrics for Case Study 3, April 26, 2014, a day with weather driven by a strong mid-latitude trough. The units of RMSE and bias are CI. The highest correlation and lowest RMSE and bias for each forecast horizon are in bold type. The ANOC ensemble mean and control forecasts have the lowest RMSE for all forecasts horizons. The forecast based on dense optical flow has a lower RMSE than that based NWP winds for all forecast horizons.

	Horizon	ANOC Ens. Mean	ANOC Control	Persis.	Opt. Flow	NWP Winds	NWP Avg. Winds	Radiosonde
RMSE	15	<b>0.23</b>	<b>0.23</b>	0.24	<b>0.23</b>	0.30	0.29	0.36
	30	<b>0.28</b>	0.29	0.32	0.29	0.40	0.38	0.39
	45	<b>0.29</b>	0.31	0.37	0.34	0.40	0.41	0.37
	60	<b>0.29</b>	0.32	0.38	0.35	0.39	0.39	0.35
Corr.	15	<b>0.76</b>	0.75	0.73	0.75	0.61	0.63	0.40
	30	<b>0.63</b>	0.61	0.52	0.62	0.24	0.32	0.24
	45	<b>0.60</b>	0.58	0.36	0.48	0.18	0.16	0.28
	60	<b>0.60</b>	0.56	0.35	0.49	0.23	0.27	0.40
Bias	15	-0.02	-0.02	<b>0.01</b>	0.02	-0.10	-0.08	-0.10
	30	-0.03	-0.03	<b>0.01</b>	0.04	-0.12	-0.10	-0.04
	45	-0.04	-0.04	<b>0.00</b>	0.04	-0.11	-0.10	0.01
	60	-0.07	-0.06	-0.03	0.02	-0.09	-0.07	<b>-0.01</b>

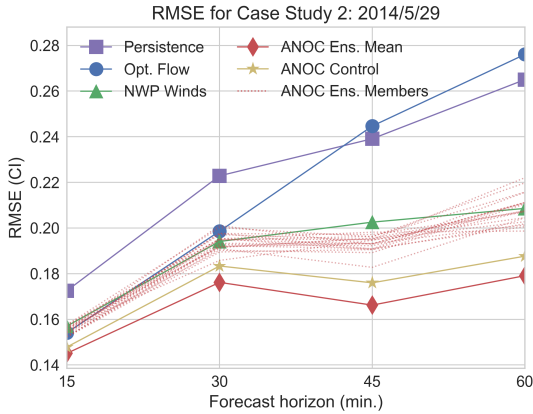


Figure 5: RMSE as a function of forecast horizon in Case Study 2 (shortwave trough). Shown are RMSE of the ANOC ensemble, ANOC ensemble mean, ANOC control, and of two reference forecast systems. The forecast based on dense optical flow has the highest RMSE. The ANOC ensemble and the forecast based on NWP winds have comparable RMSE. The ANOC ensemble mean and control forecast have the lowest RMSE.

ANOC ensemble mean and dense optical flow forecasts contain a thick cloud in the upper portion of the domain. In the same part of the domain, the clouds produced by the forecast based on NWP winds are thinner. This occurs because, as the radiosonde indicates, there are two cloud layers moving at different speeds. The forecast based on NWP winds sometimes uses winds from the the high-altitude level (contains the fast moving cirrus) but other times uses winds from the mid-altitude level (contains the slower moving mid-altitude clouds). This problem is avoided in ANOC by assimilating sparse optical flow vectors in addition to the CMV

fields from the NWP model.

#### 5.4. Case study summary

In all three case studies, the daily RMSE of the ANOC ensemble mean is lower than those of the reference forecasts for all forecast horizons (15, 30, 45, and 60 minutes). The precise value of daily RMSE, however, varies between days. When the weather is dominated by advection (Case Study 1), all forecasts with time dependent CMV fields (NWP spatially averaged winds, NWP winds, dense optical flow, and ANOC) yield better forecasts, in terms of the performance metrics, than the persistence or radiosonde forecasts. Whether forecasts based on dense optical flow or those based on NWP winds have lower RMSE depends on the weather conditions: in Case Study 2 (shortwave trough), the NWP based forecasts are better than those based on dense optical flow, but in Case Study 3 (mid-latitude trough), dense optical flow leads to better forecasts than forecasts based on the NWP model. The ANOC forecast system combines the strength of both techniques and leads to better forecasts, but requires an increase in computational requirements and conceptual complexity.

Finally, recall that the ANOC ensemble mean forecast results in a smoother forecast (Fig. 3) with a lower standard deviation, and lower RMSE than the ANOC ensemble members and ANOC control (see Figs. 5 and 7). RMSE can be decomposed as

$$\text{RMSE} = \sqrt{\sigma_f^2 + \sigma_t^2 - 2\sigma_f\sigma_t\text{Corr.} + \text{Bias}^2}, \quad (10)$$

where  $\sigma_f$  is the standard deviation of the forecast and  $\sigma_t$  is the standard deviation of the observed CI

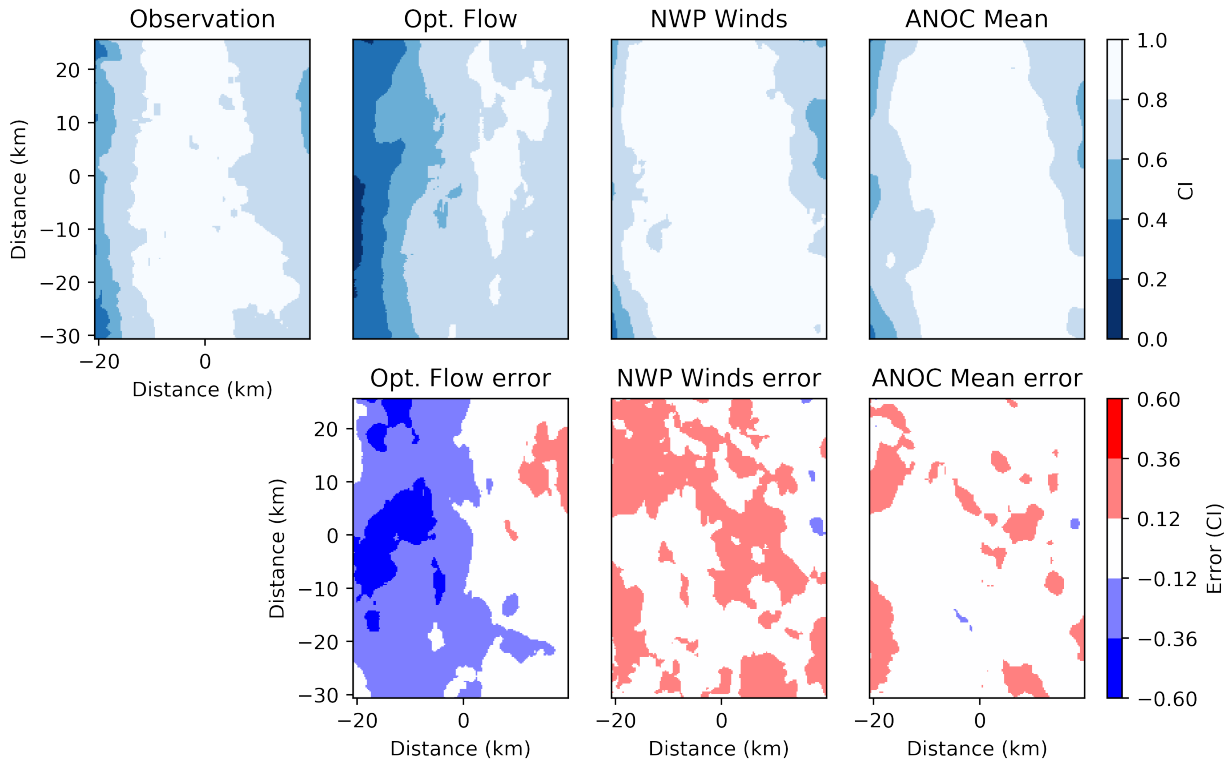


Figure 6: Forecasts and errors in Case Study 2, May 29, 2014, at 12:15 MST. The forecast horizon is 30 minutes. Top row, left to right: satellite derived CI field at 12:15 MST, and forecasts based on dense optical flow, NWP winds and ANOC. Bottom row: error fields corresponding to each forecast. The forecast based on dense optical flow does not correctly advect the cloud edge and thins the cloud, leading to poor performance metrics compared to ANOC or NWP wind based forecasts.

755 field. Therefore, increasing smoothness (decreasing  $\sigma_f$ ) can reduce RMSE.

The lower RMSE of the ANOC ensemble mean compared to the ANOC control suggests some of the reduction is a result of increased smoothness. Case Studies 2 and 3, however, suggest that smoothing is not the only source of the reduced RMSE. In Case Study 2, ANOC’s ensemble members all yield a lower RMSE than the forecast based on dense optical flow (see Fig. 5) and the ensemble members are not smoothed. In the same case study, the ANOC control forecast has a lower RMSE than the forecast based on dense optical flow or NWP winds and also does not have a smoothed CI field. In Case Study 3, ANOC’s ensemble members and control forecast yield a lower RMSE than forecasts based only on the NWP model for all horizons. In the same case study, the RMSEs of the ANOC ensemble members and control forecast are comparable to the RMSE of the forecast based on dense optical flow at the 15 and 30 minute horizons, but

lower at the 45 and 60 minute horizons (see Fig. 7).

The choice between using the ANOC ensemble mean or the ANOC control forecast comes down to a choice between smoothness and RMSE. If an application requires a forecast with low RMSE but does not require a field with realistically sharp cloud edges, then the ensemble mean may be a better forecast. If, however, the sharpness of the cloud edges is critical (e.g. forecasting ramp rates) then the control forecast may be more valuable.

## 6. Analysis over 3 months

We compute performance metrics over 39 days taken from April, May, and June of 2014. We only consider days where cloud cover is detected. We manually inspect the satellite images over the three month period. Days with at least one image with (even a small amount of) cloud coverage are included. Thus, while all 39 days have some amount of cloud cover at some point during the day, there are periods that are free of cloud coverage.

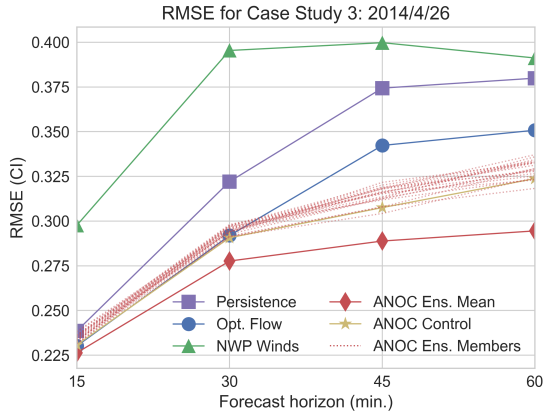


Figure 7: RMSE as a function of forecast horizon in Case Study 3 (mid-latitude trough). Shown are RMSE of the ANOC ensemble, ANOC ensemble mean, ANOC control, and of two reference forecast systems. The forecast based on NWP winds has the highest RMSE. The forecast based on dense optical flow is comparable to the ANOC forecasts for 15 and 30 minute horizons. RMSE of the forecast based on dense optical flow is larger than RMSE of the ANOC ensemble and control forecast for 45 and 60 minute horizons.

We first consider the RMSE for each of the 39 individual days. The results are shown in Fig. 9. We highlight four observations from these results.

1. The ANOC ensemble mean tends to have a daily RMSE lower than the forecast based on NWP winds or the forecast based on dense optical flow.
2. The improvement in RMSE for the ANOC ensemble mean is more significant for days in which the RMSE of all forecasts is relatively high (above 0.5 CI for instance).
3. The ANOC ensemble mean typically leads to a better forecasts for longer horizons. For example, for the 15 minute forecast horizon, there are 12 days for which the ANOC ensemble mean has an RMSE above 0.1. Of these 12 days the ANOC ensemble mean has the lowest RMSE for 8. For the 60 minute horizon, there are 18 days for which the ANOC ensemble mean has an RMSE above 0.1, and the ANOC ensemble mean has a lower RMSE for all of them. This may be due to an increase in ensemble spread at longer forecast horizons leading to greater smoothing.
4. The two ANOC forecasts perform similarly to the more established reference forecasts on all days suggesting that the ANOC method is a useful technique.

Performance metrics, averaged over 39 days, are listed in Table 4. The ANOC ensemble mean has a lower RMSE and higher correlation than all other forecast systems. The ANOC control forecast performs almost the same as the forecasts based on dense optical flow and NWP winds in terms of both RMSE and correlation. The bias of all the forecasts are nearly zero apart from the forecasts based on NWP or radiosonde winds, though these are low as well.

The RMSE skill scores (persistence serves as the reference) of the ANOC ensemble mean, ANOC control, the forecast based on NWP winds, and the dense optical flow forecast are listed in Table 5. The ANOC ensemble mean forecast skill increases with forecast horizon. The ANOC control forecast skill is fairly consistent over time. The skill of the forecast based on dense optical flow, however, decreases with the forecast horizon. The skill of the forecast based on NWP winds is lower, but does not change with forecast horizon.

These skill score results are intuitive. Dense optical flow used here is based on the movement of clouds over a 15 minute period. The CMV fields from dense optical flow will therefore be sensitive to the dynamics over this shorter time scale. It is expected that skill scores of forecasts based on these CMV fields will decrease with forecast horizon. The short term nature of the dense optical flow CMV fields is not found in the NWP model. This can partially explain why the skill scores based on NWP winds does not increase with forecast horizon. The NWP model we use is initialized at 12Z and does not assimilate observations throughout the day. It is thus reasonable that the skill score of forecasts based on NWP winds is relatively low since it does not use more recent information from the satellite images.

The ANOC system uses DA to combine both of these sources of information based on the relative uncertainty assigned to each. For that reason, expected that the ensemble mean and control forecast have a higher skill for all the horizons than either the NWP winds or dense optical flow forecasts. The skill of the ANOC ensemble mean increases with the forecast horizon, while the ANOC control forecast decreases slightly. Ensemble means often have a larger skill than control forecasts over longer forecast horizons (Kalnay, 2003), but some of the skill increase of the ensemble mean can be attributed to increased smoothness. This smoothing is based on the uncertainty of the underlying system.

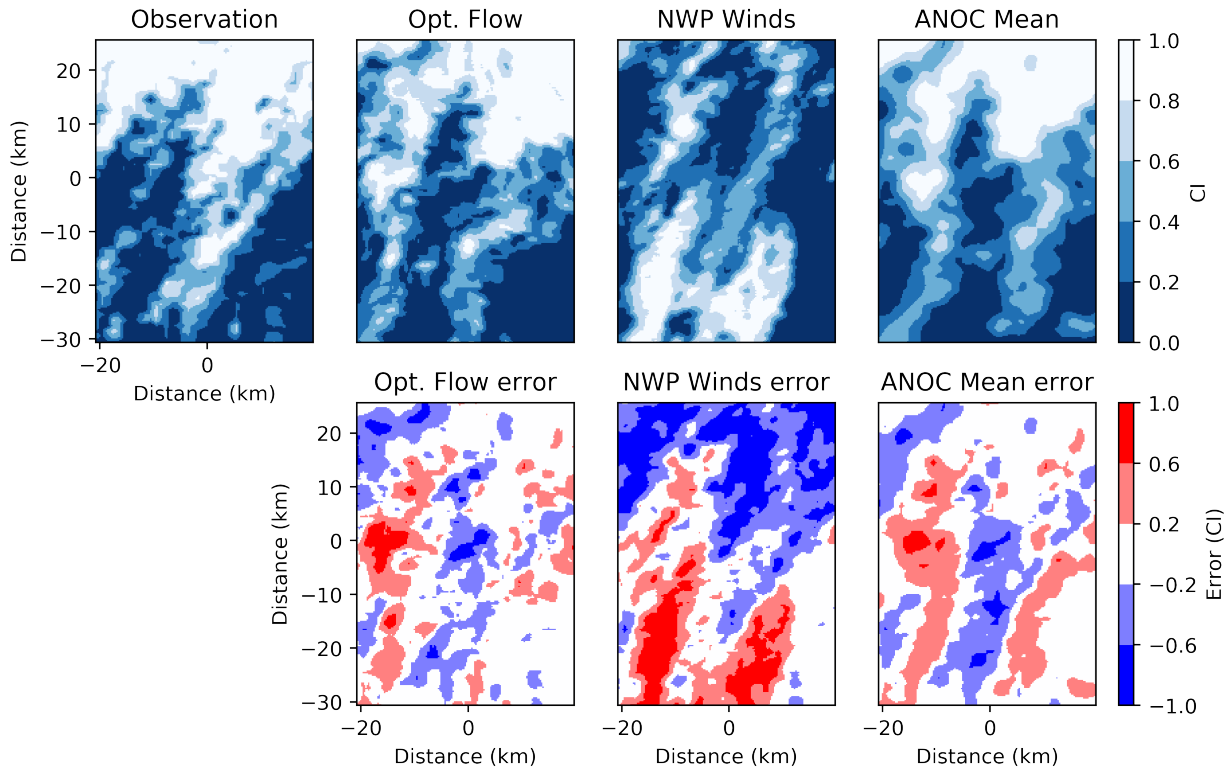


Figure 8: Forecasts and errors in Case Study 3, April 26, 2014, at 13:00 MST. The forecast horizon is 30 minutes. Top row, left to right: satellite derived CI field at 13:00 MST, and forecasts based on dense optical flow, NWP winds and the ANOC ensemble mean. Bottom row: error fields corresponding to each forecast. The NWP winds forecast does not correctly advect the clouds on this day due to the presence of two cloud levels and two local maxima in relative humidity. The ANOC system corrects the NWP based CMV field by assimilating sparse optical flow CMVs.

Figure 10 illustrates average RMSE of ANOC ensemble mean and control, forecast based on dense optical flow, and forecast based on NWP winds. Average RMSE exhibits a pattern familiar from the case studies: RMSE of ANOC ensemble mean is lower than RMSE of forecasts based on dense optical flow or NWP winds. While the RMSE of all methods increases with forecast horizon, the RMSE of the ANOC ensemble mean increases at the slowest rate. The ANOC control forecast performs similarly to the optical flow forecast as 15 and 30 minute forecasts, but has a lower RMSE at 45 and 60 minute horizons.

## 7. Conclusion

We introduced the ANOC forecast system for intra-hour forecasts of CI over the area of a city. ANOC uses a conceptually simple forecast model, and combines CMV data based on the uncertainties

associated with each data source using data assimilation.

We validated the ANOC system by comparing it to reference forecasts techniques. Our comparisons are based on a standard set of performance metrics. We considered three representative case studies and found that the ANOC forecasts perform similarly or better, in terms of the performance metrics, than the reference forecast techniques. This comes at the cost of an increase in computational requirements and conceptual complexity. We also considered performance metrics over 39 days to confirm our conclusions from the case studies. The results suggest that ANOC, or similar DA based systems, can be useful in intra-hour forecasting for solar power applications.

The ANOC ensemble mean is smoother than the reference forecasts, and is smoother than the true CI fields. This smoothness is caused by ensemble spread. Quantifying the relationship between en-

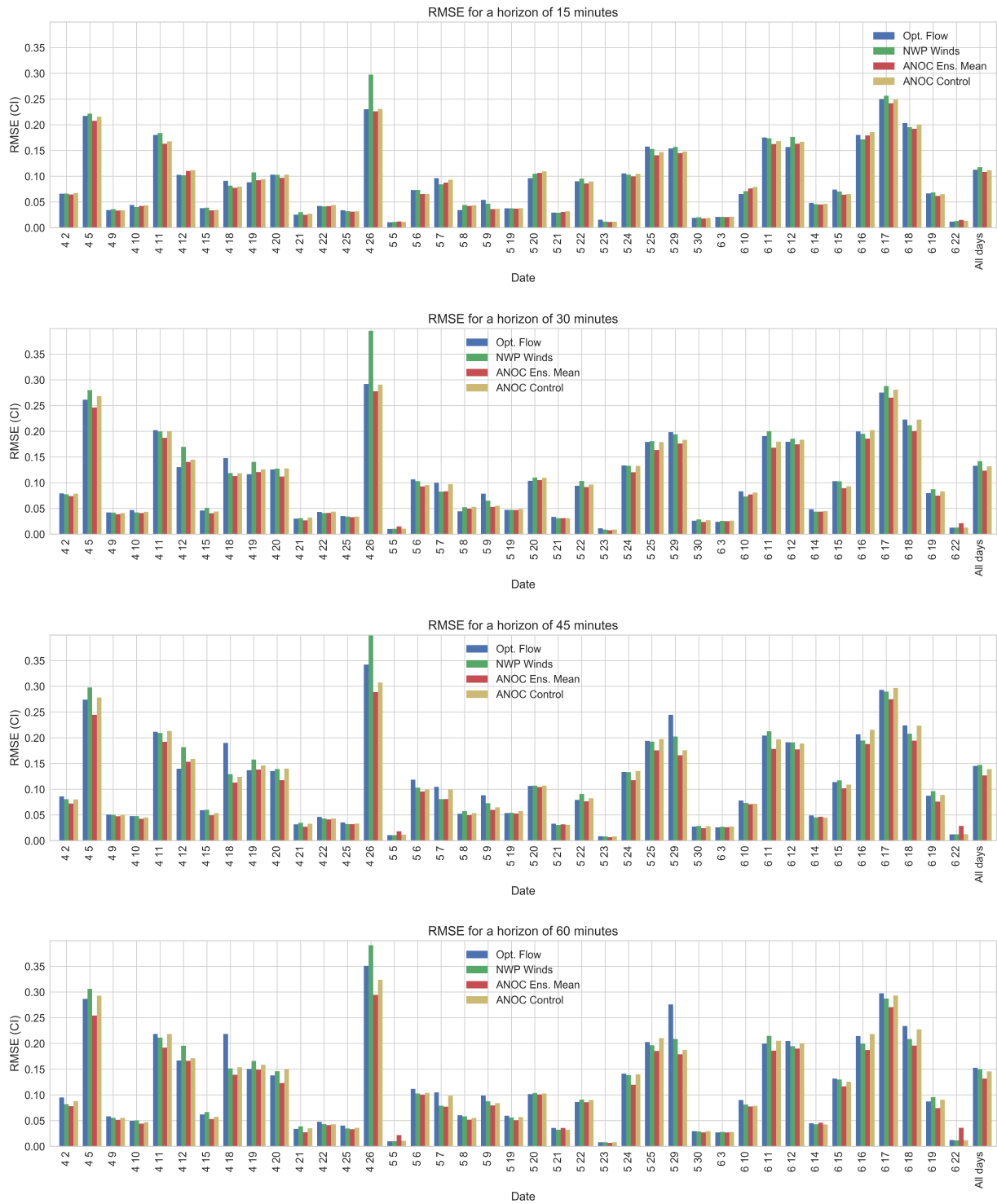


Figure 9: Bar charts of daily RMSE (measured in units of CI) for the ANOC ensemble mean and control, and forecasts using dense optical flow and NWP winds for forecast horizons of 15, 30, 45, and 60 minutes for each cloudy day and all cloudy days for the study period. The ANOC forecast typically has the lowest RMSE of all three methods when all methods yield a large RMSE, e.g., 4/5, 4/26 or 6/17. The ANOC forecast sometimes has a higher RMSE than the reference forecasts when all methods yield a low RMSE, e.g., 5/5 or 6/22. The forecast methods tend to produce similar results.



Table 4: Performance metrics averaged over 39 days. The units of RMSE and bias are CI. The highest correlation and lowest RMSE and bias for each forecast horizon are in bold type. The ANOC control forecast performs very similarly to the forecasts based on optical flow and those based on NWP winds. The ANOC ensemble mean forecast has the lowest RMSE for all forecasts horizons, though it performs similarly to the reference forecasts.

	Horizon	ANOC Ens. Mean	ANOC Control	Persis.	Opt. Flow	NWP Winds	NWP Avg. Winds	Radiosonde
RMSE	15	<b>0.11</b>	<b>0.11</b>	0.12	<b>0.11</b>	0.12	0.12	0.14
	30	<b>0.12</b>	0.13	0.14	0.13	0.14	0.14	0.15
	45	<b>0.13</b>	0.14	0.15	0.15	0.15	0.15	0.16
	60	<b>0.13</b>	0.15	0.16	0.15	0.15	0.15	0.16
Corr.	15	<b>0.88</b>	0.87	0.84	0.87	0.85	0.86	0.80
	30	<b>0.84</b>	0.82	0.79	0.82	0.79	0.79	0.75
	45	<b>0.83</b>	0.80	0.76	0.78	0.77	0.76	0.73
Bias	60	<b>0.81</b>	0.77	0.74	0.75	0.76	0.75	0.71
	15	<b>0.00</b>	<b>0.00</b>	<b>0.00</b>	<b>0.00</b>	-0.01	-0.01	-0.01
	30	<b>0.00</b>	-0.01	<b>0.00</b>	<b>0.00</b>	-0.02	-0.02	-0.01
	45	<b>-0.01</b>	<b>-0.01</b>	<b>-0.01</b>	<b>-0.01</b>	-0.02	-0.02	-0.02
	60	<b>-0.01</b>	<b>-0.01</b>	<b>-0.01</b>	<b>-0.01</b>	-0.02	-0.02	-0.02

Table 5: RMSE skill scores averaged over 39 days (reference is persistence forecast). The highest skill score for each forecast horizon is in bold type. The ANOC Ensemble mean and control forecasts have a higher skill for all forecast horizons. The ANOC ensemble mean forecast skill grows at a faster rate than the other forecasting methods as the forecast horizon increases.

Horizon	ANOC Ens. Mean	ANOC Control	Opt. Flow	NWP Winds
15	<b>0.12</b>	0.10	0.09	0.05
30	<b>0.14</b>	0.08	0.07	0.01
45	<b>0.17</b>	0.09	0.05	0.04
60	<b>0.16</b>	0.08	0.03	0.05

semble spread and forecast uncertainty or skill is left for future work.

Each individual ensemble member and the control forecast of the ANOC is not smoothed. A smooth CI forecast produces a smooth power forecast, this results in ramp rates that are underestimated. We can therefore use individual ensemble members and the control forecast rather than the ensemble mean to predict the amplitude of ramp events. The control forecast is the best prediction of the ramp event, and the individual ensemble members could provide information on the uncertainty of the magnitude and timing of the ramp event.

In summary, ANOC’s forecasts are on average similar or better, in terms of the performance metrics, than the reference forecasts. This conclusion is based on averages computed over a three month period and over a domain centered on Tucson, AZ. Further study is needed to determine if the ANOC system will perform similarly in other parts of the country or during a different time of the year over Tucson. Our study, however, indicates that ANOC, or systems similar to ANOC, are computationally

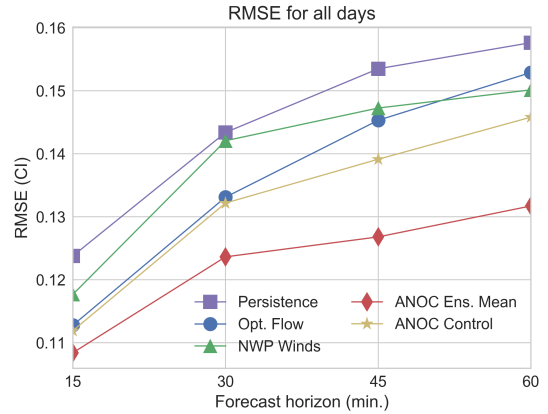


Figure 10: Average RMSE as a function of forecast horizon for ANOC ensemble mean and control, forecasts based on dense optical flow and forecasts based on NWP winds. The ANOC forecast yields lower RMSE than the other forecast techniques. For the large forecast horizons, RMSE of the forecast based on NWP winds is lower than RMSE of the forecast based on dense optical flow.

feasible and further developments for an ensemble based DA framework in this context is promising.

## Acknowledgments

Funding for this work was provided in part by Tucson Electric Power and Arizona Public Service. MM and TMH gratefully acknowledge support by the National Science Foundation (grant DMS-1619630). MM gratefully acknowledges support by the Office of Naval Research (grant number N00173-17-2-C003) and by the Alfred P. Sloan Foundation (Sloan Research Fellowship).



The authors thank Michael Leuthold for help with the WRF model. The authors thank Michael Leuthold and Eric Betterton for discussion and input.

## References

- Alnæs, M.S., Blechta, J., Hake, J., Johansson, A., Kehlet, B., Logg, A., Richardson, C., Ring, J., Rognes, M.E., Wells, G.N., 2015. The fenics project version 1.5. *Archive of Numerical Software* 3. doi:10.11588/ans.2015.100.20553.
- Asch, M., Bocquet, M., Nodet, M., 2016. *Data Assimilation: Methods, Algorithms, and Applications*. SIAM, Philadelphia, PA. doi:10.1137/1.9781611974546.
- Bradski, G., 2000. *The OpenCV Library*. Dr. Dobb's Journal of Software Tools .
- Burgers, G., van Leeuwen, P., Evensen, G., 1998. Analysis scheme in the ensemble Kalman filter. *Monthly Weather Review* 126, 1719–1724. doi:10.1175/1520-0493(1998)126<1719:ASITEK>2.0.CO;2.
- Côté, S., Tatnall, A.R., 1995. A neural network-based method for tracking features from satellite sensor images. *International Journal of Remote Sensing* 16, 3695–3701. doi:10.1080/01431169508954656.
- Descombes, G., Auligné, T., Lin, H.c., Schwartz, C.S., 2014. Multi-sensor advection diffusion nowCast (MAD-Cast) for cloud analysis and short-term prediction. Technical Report NCAR/TN 509+STR. NCAR, Boulder, CO. doi:10.5065/D62V2D37.
- Evensen, G., 2009. *Data Assimilation: The Ensemble Kalman Filter*. Springer, Berlin and Heidelberg, Germany. doi:10.1007/978-3-642-03711-5.
- Guillot, E.M., Vonder Haar, T.H., Forsythe, J.M., Fletcher, S.J., 2012. Evaluating satellite-based cloud persistence and displacement nowcasting techniques over complex terrains. *Weather and Forecasting* 27, 502–514. doi:10.1175/WAF-D-11-00037.1.
- Hammer, A., Heinemann, D., Lorenz, E., Lücke, B., 1999. Short-term forecasting of solar radiation: a statistical approach using satellite data. *Solar Energy* 67, 139–150. doi:10.1016/S0038-092X(00)00038-4.
- Harty, T.M., 2018. Geostationary satellite images centered around Tucson, AZ. URL: [https://sandbox.zenodo.org/record/252109#.w\\_LqiHWnGak](https://sandbox.zenodo.org/record/252109#.w_LqiHWnGak).
- Haupt, S.E., Kosović, B., Jensen, T., Lazo, J.K., Lee, J.A., Jiménez, P.A., Cowie, J., Wiener, G., Mccandless, T.C., Rogers, M., Miller, S., Sengupta, M., Xie, Y., HinKeLman, L., KaLb, P., Heiser, J.H., 2018. Building the SUN4CAST system. *Bulletin of the American Meteorological Society* 99, 121–135. doi:10.1175/BAMS-D-16-0221.1.
- Horn, B.K.P., Schunck, B.G., 1981. Determining optical flow. *Artificial Intelligence* 17, 185–203. doi:10.1016/0004-3702(81)90024-2.
- Hunt, B.R., Kostelich, E.J., Szunyogh, I., 2007. Efficient data assimilation for spatiotemporal chaos: A local ensemble transform Kalman filter. *Physica D: Nonlinear Phenomena* 230, 112–126. doi:10.1016/j.physd.2006.11.008.
- Kalnay, E., 2003. *Atmospheric Modeling, Data Assimilation and Predictability*. Cambridge university press, Cambridge. doi:10.1017/CB09780511802270.
- Kleissl, J., 2013. *Solar energy forecasting and resource assessment*. Academic Press, Oxford, United Kingdom and Waltham, MA. doi:10.1016/B978-0-12-397177-7.18001-5.
- Lave, M., Kleissl, J., 2013. Cloud speed impact on solar variability scaling - application to the wavelet variability model. *Solar Energy* 91, 11–21. doi:10.1016/j.solener.2013.01.023.
- Logg, A., Mardal, K.A., Wells, G.N., et al., 2012. *Automated Solution of Differential Equations by the Finite Element Method*. Springer, Berlin and Heidelberg, Germany. doi:10.1007/978-3-642-23099-8.
- Lorenz, E., Hammer, A., Heinemann, D., 2004. Short term forecasting of solar radiation based on satellite data, in: *EUROSUN2004 (ISES Europe Solar Congress)*, pp. 841–848. URL: [https://www.researchgate.net/profile/Annette\\_Hammer/publication/267971482\\_Short\\_term\\_forecasting\\_of\\_solar\\_radiation\\_based\\_on\\_satellite\\_data/links/5583ecb708ae4738295bb661.pdf](https://www.researchgate.net/profile/Annette_Hammer/publication/267971482_Short_term_forecasting_of_solar_radiation_based_on_satellite_data/links/5583ecb708ae4738295bb661.pdf).
- Lorenzo, A.T., Morzfeld, M., Holmgren, W.F., Cronin, A.D., 2017. Optimal interpolation of satellite and ground data for irradiance nowcasting at city scales. *Solar Energy* 144, 466–474. doi:10.1016/j.solener.2017.01.038.
- Lucas, B.D., Kanade, T., 1981. An iterative image registration technique with an application to stereo vision, in: *Proceedings DARPA Image Understanding Workshop*, pp. 674–679. URL: [https://ri.cmu.edu/pub\\_files/pub3/lucas\\_bruce\\_d\\_1981\\_2/lucas\\_bruce\\_d\\_1981\\_2.pdf](https://ri.cmu.edu/pub_files/pub3/lucas_bruce_d_1981_2/lucas_bruce_d_1981_2.pdf).
- Menzel, W.P., 2001. Cloud tracking with satellite imagery: from the pioneering work of Ted Fujita to the present. *Bulletin of the American Meteorological Society* 82, 33–47. doi:10.1175/1520-0477(2001)082<0033:CTWSIF>2.3.CO;2.
- Miller, S., Rogers, M., Heidinger, A., Laszlo, I., Sengupta, M., 2012. Cloud advection schemes for short-term satellite-based insolation forecasts, in: *Proceedings of the World Renewable Energy Forum, American Solar Energy Society*. pp. 1963–1967. URL: [https://ases.conference-services.net/resources/252/2859/pdf/SOLAR2012\\_0385\\_full%20paper.pdf](https://ases.conference-services.net/resources/252/2859/pdf/SOLAR2012_0385_full%20paper.pdf).
- Miller, S.D., Rogers, M.A., Haynes, J.M., Sengupta, M., Heidinger, A.K., 2017. Short-term solar irradiance forecasting via satellite/model coupling. *Solar Energy* doi:10.1016/j.solener.2017.11.049.
- Nieman, S.J., Menzel, W.P., Hayden, C.M., Gray, D., Wanzong, S.T., Velden, C.S., Daniels, J., 1997. Fully automated cloud-drift winds in NESDIS operations. *Bulletin of the American Meteorological Society* 78, 1121–1133. doi:10.1175/1520-0477(1997)078<1121:FACDWI>2.0.CO;2.
- NOAA, 2018. Comprehensive large array-data stewardship system (class). <https://www.av1.class.noaa.gov/saa/products/welcome>. Accessed: 2018-11-28.
- Nonnenmacher, L., Coimbra, C.F.M., 2014. Streamline-based method for intra-day solar forecasting through remote sensing. *Solar Energy* 108, 447–459. doi:10.1016/j.solener.2014.07.026.
- Peng, Z., Yoo, S., Yu, D., Huang, D., 2013. Solar irradiance forecast system based on geostationary satellite, in: *2013 IEEE International Conference on Smart Grid Communications (SmartGridComm)*, pp. 708–713. doi:10.1109/SmartGridComm.2013.6688042.
- Perez, R., Ineichen, P., Moore, K., Kmiecik, M., Chain, C., George, R., Vignola, F., 2002. A new operational model for satellite-derived irradiances: description and validation. *Solar Energy* 73, 307–317. doi:10.1016/

- 1075 S0038-092X(02)00122-6.  
Reich, S., Cotter, C., 2015. Probabilistic Forecasting and Bayesian Data Assimilation. Cambridge University Press, Cambridge, United Kingdom. doi:10.1017/CB09781107706804.
- 1080 Snyder, J.P., 1987. Map Projections: A Working Manual. US Government Printing Office, Washington, DC. doi:10.3133/pp1395.
- Sun, D., Roth, S., Black, M.J., 2010. Secrets of optical flow estimation and their principles, in: Proceedings of the IEEE Computer Society Conference on Computer Vision and Pattern Recognition, pp. 2432–2439. doi:10.1109/CVPR.2010.5539939.
- 1085 TEP, 2018. Our renewable resources. <https://www.tep.com/renewable-resources-2/>. Accessed: 2018-11-13.
- 1090 Toth, Z., Kalnay, E., 1997. Ensemble forecasting at ncep and the breeding method. Monthly Weather Review , 3297–3319doi:10.1175/1520-0493(1997)125<3297:EFANAT>2.0.CO;2.
- 1095 Wicker, L.J., Skamarock, W.C., 2002. Time-splitting methods for elastic models using forward time schemes. Monthly Weather Review 130, 2088–2097. doi:10.1175/1520-0493(2002)130<2088:TSMFEM>2.0.CO;2.
- 1100 Wilks, D., 2011. Chapter 8 - forecast verification, in: Wilks, D.S. (Ed.), Statistical Methods in the Atmospheric Sciences. Academic Press, Oxford, United Kingdom and Waltham, MA. volume 100 of *International Geophysics*, pp. 301 – 394. doi:10.1016/B978-0-12-385022-5.00008-7.
- 1105 Wolff, B., Kühnert, J., Lorenz, E., Kramer, O., Heine-  
mann, D., 2016. Comparing support vector regression for PV power forecasting to a physical modeling approach using measurement, numerical weather prediction, and cloud motion data. Solar Energy 135, 197–208. doi:10.1016/j.solener.2016.05.051.